Electromagnetic shielding properties of LPBF produced Fe2.9wt.%Si alloy

Journal of Physics: Energy

PAPER

Electromagnetic shielding properties of LPBF produced Fe2.9wt.%Si alloy

Michele Quercio[1,4], Francesco Galbusera[2,4], Aldo Canova[1], Ali Gökhan Demir[2,*], Giambattista Gruosso[3] and Barbara Previtali[2]

[1] Energy Department, Politecnico di Torino, Turin, Italy
[2] Department of Mechanical Engineering, Politecnico di Milano, Milan, Italy
[3] Department of Electronics, Information and Bioengineering, Politecnico di Milano, Milan, Italy
[4] The authors MQ and FG contributed equally to this work.
[*] Author to whom any correspondence should be addressed.

E-mail: aligokhan.demir@polimi.it

Keywords: electromagnetic shielding, electrical motors, laser powder bed fusion, Fe-Si alloys

OPEN ACCESS

RECEIVED
21 March 2023

REVISED
5 June 2023

ACCEPTED FOR PUBLICATION
20 July 2023

PUBLISHED
10 August 2023

Abstract

Ferromagnetic materials are used in various applications such as rotating electrical machines, wind turbines, electromagnetic shielding, transformers, and electromagnets. Compared to hard magnetic materials, their hysteresis cycles are featured by low values of coercive magnetic field and high permeability. The application of additive manufacturing to ferromagnetic materials is gaining more and more attraction. Indeed, thanks to a wider geometrical freedom, new topological optimized shapes for stator/rotor shapes can be addressed to enhance electric machines performances. However, the properties of the laser powder bed fusion (LPBF) processed alloy compared to conventionally produced counterpart must be still addressed. Accordingly, this paper presents for the first time the use of the LPBF for the manufacturing of Fe2.9wt.%Si electromagnetic shields. The process parameter selection material microstructure and the magnetic shielding factor are characterized.

1. Introduction

The additive manufacturing (AM) technologies market is constantly growing as reported in [1, 2]. One of the recent application fields of AM is the e-mobility industry, where the constant need of electric machines development and optimization perfectly matches with the potentialities enabled by AM technologies [3–10]. Among others, laser powder bed fusion (LPBF) emerges as one of the most suitable AM processes to deal with the e-mobility materials [11–13]. As a matter of fact, thanks to the action of a laser beam with spots typically less than 100 μm, the production of 3D parts with intricate shapes and designs is enabled, such as ferromagnetic iron cores with engineered flux path [4–6, 8, 14] or aluminum/copper windings with custom shapes and integrated cooling channels to maximize the performances of next-generation electric motors [4–8, 15]. Specifically, to produce soft magnetic iron cores, which find innumerous applications for rotors [16, 17], stators [18, 19], transformers [20, 21] or linear actuators [5], the most common alloys employed are Fe-Si (electrical steel), Fe-Ni or Fe-Co alloys, ferrites and amorphous alloys. The choice of the alloy composition highly depends on the tradeoff between price and magnetic properties achievable. In the low-frequency application spectrum (50–60 Hz), the combination of low price, low power losses and high saturation polarization and permeability of electrical steels justifies their extensive use in the production of electromagnetic devices [8, 22–24]. For low frequency applications Fe-Ni/Fe-Co alloys can be used [25–27], but usually at the expense of a higher purchase price or lower magnetic properties. Instead, at high frequency applications (kHz–MHz), amorphous and nanocrystalline materials exhibit superior magnetic properties that justify their higher cost [8, 27].

The highest maturity level in terms of LPBF processability has been reached with electrical steel compositions [8]. So far, several works have been published with Fe2.9wt.%Si [28–30], Fe3wt.%Si [20, 22, 24, 31], Fe3.7wt.%Si [32, 33], Fe6.5wt.%Si [20, 23, 31, 34, 35], Fe6.7wt.%Si [36], Fe6.9wt.%Si [37–40],

demonstrating that highly dense parts with good spatial accuracy can be produced [4]. High-temperature post annealing treatments are often required to match the magnetic properties of the final artifacts to the acceptable standards [38]. Typically, a rising Si-content in the composition of electrical steels allows to significantly improve their magnetic properties, however its content increases the cracking susceptibility. Recently, controlled stochastic cracking has been investigated as a viable way to better manipulate the magnetic properties of Fe6.5wt.%Si, even though for structural parts cracking represents a detrimental issue [34]. Other woks demonstrated that LPBF can be successfully adopted to realize large scale prototypes, such as rotors for electric motors [29, 30, 32, 41, 42] or transformers [20, 21] made of electrical steels. An innovative application for these materials is the production of electromagnetic shields. These devices are used to shield the most delicate parts of electronic equipment (such as aircraft instrumentation) from external harmful electromagnetic wave sources. Complex maze-like structures such as lattice or honeycomb can be easily realized via LPBF to increase the number of surfaces that contribute to the shielding from electromagnetic waves while simultaneously reducing the weight of these objects, which is extremely desirable in the aerospace field. Some studies focused on the LPBF realization of complex shape shields made of Ni-Fe-Mo alloys [43–46] and their functional characterization in terms of shielding performance [43, 44] have been published so far. However, none of these was realized with electrical steels, which stand out as the most processed soft magnetic alloy in the literature.

Accordingly, the purpose of the present work is to evaluate the magnetic performances of Fe2.9wt.%Si shields produced via LPBF in comparison with a Zn-coated mild steel one realized with a conventional manufacturing route. The feedstock was chosen as the representative soft magnetic material because of its relatively good magnetic properties and its remarkable lower tendency to develop cracks during LPBF process in comparison with electrical steels with higher Si-content. The benchmarking work is carried out using simple geometries to compare the conventional manufacturing route to AM route with a dedicated alloy. Initially, process parameters were tuned to match high densification (>99.9%) for the as-built samples with a dedicated experimental campaign. With the chosen parameter combination, the microstructure was studied in as-built and heat treated conditions [38]. The magnetic properties of the additively manufactured specimens were characterized, and the extracted parameters were used to simulate the shielding factor. Experimentally the shielding factor was validated and compared with the conventionally produced component.

2. Simulation of the shielding system

The shielding properties of the system were evaluated through experimental campaigns and the results compared with the values of the simulations conducted on the same system. The simulations were performed using the COMSOL software. The apparatus which has been simulated is shown in figure 1 and represents the tested case of figure 4(a).

The cases presented refer to alternating current tests, using as source an inductor formed by 25 turns crossed by a current of 1 A. To simplify the simulation, a homogeneous multi-turns system has been considered by designing a hollow cylinder as inductor instead of the individual turns. A measure of the effectiveness of a shield in reducing the magnitude of the magnetic field at a given point is the shielding factor SF [47, 48], defined as:

$$SF = \frac{|B_0(x,y,z)|}{|B_S(x,y,z)|} \tag{1}$$

where B_0 is the magnetic induction at a certain point when the shield is absent, B_S is the equivalent with the shield applied. For this reason, several simulations have been conducted without and with the presence of the shield. The SF values were taken at the three points of interest as indicated in figure 4(b). The simulations were carried out using electromagnetic properties of the additively manufactured samples in as-built and heat treated conditions through the experimental analysis.

3. Materials and methods

3.1. Fe-Si alloy powder

Throughout the experimental activity, a feedstock of gas atomized low—silicon steel powder (m4p material solutions GmbH, Austria) was processed. The nominal chemical composition consisted of 2.9 wt.% Si and Fe bal. The declared powder granulometry was comprised between 20 and 53 μm with a spherical morphology as shown in figure 2.

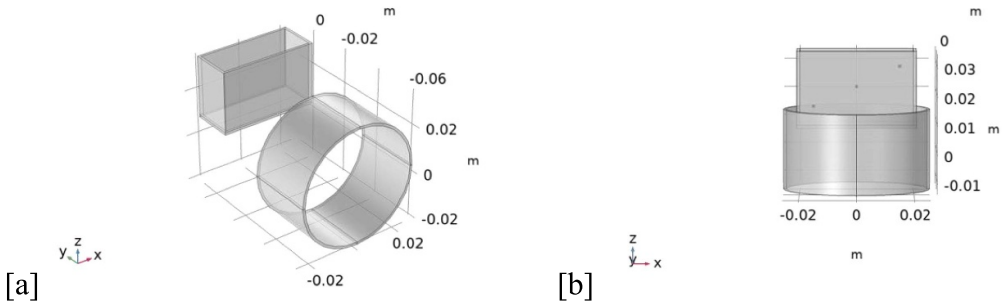

Figure 1. CAD of the shielding system (a) magnetic field source on *Z* direction, (b) magnetic field source on *Y* direction.

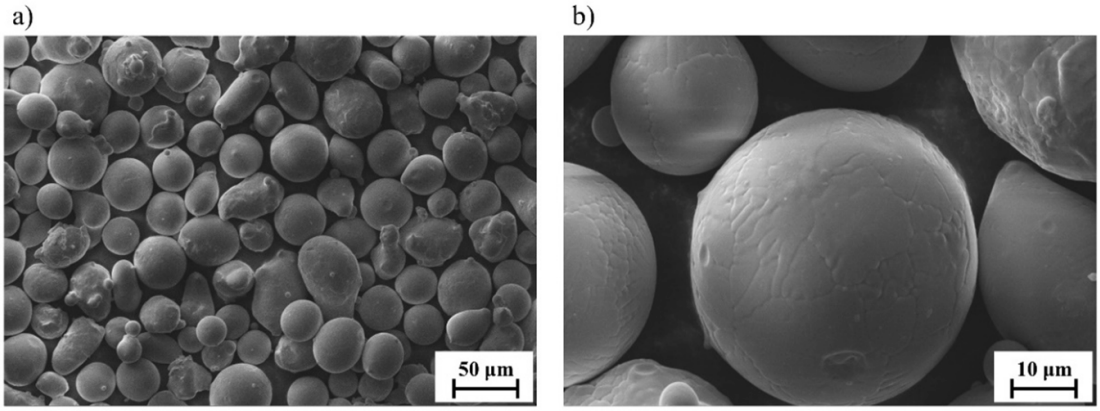

Figure 2. (a) SEM images of the Fe2.9wt.%Si powder feedstock; (b) detail of a spherical particle.

3.2. LPBF system

An industrial LPBF system with an open architecture (LLA150R, 3D-NT, Solbiate Olona, Italy) was used throughout this work. The system was equipped with a novel multi-core fiber laser source (Corona nLIGHT AFX1000, nLIGHT Inc, Vancouver, Washington, USA) capable of emitting a maximum power of 1.2 kW. The laser source guaranteed a theoretical waist diameter of 47 μm in the focus position using a Gaussian power distribution within the beam. The entire LPBF architecture was controlled by a tailored made software developed for laser applications (Direct Machining Control, Vilnius, Lithuania) to control process parameters down to the scan vector level. During building, the O_2 content was kept at 2300 ppm by purging and filling the build chamber with Ar in overpressure. Specimens and shields were built upon a conventional stainless-steel baseplate.

3.3. Experimental campaign for determining the LPBF process parameters

An experimental campaign was designed to investigate the correct LPBF feasibility window of Fe2.9wt.%Si alloy and determine adequate process parameters for the manufacturing of magnetic shields. For this purpose, small cubes with dimensions $5 \times 5 \times 5$ mm^3 were built using a constant hatch spacing and layer thickness (70 and 30 μm respectively) while varying laser power and scan speed, as shown in table 1. Two laser power levels, 150 and 200 W, were tested, along with a large spectrum of scan speeds, from 700 to 1200 mm s^{-1} with a step increase of 100 mm s^{-1}, to understand the LPBF processability of the Fe2.9wt.%Si alloy. The laser beam locally melted the powder following a bidirectional (zig–zag) pattern. The hatching was also rotated by 67° each layer. Contours were also performed with the same process parameters of the hatching. As-built cubes were then prepared following standard metallographic preparation.

3.4. Metallographic procedures

Polished metallographic cross sections of the as-built cubes were acquired with an optical microscope (Mitutoyo, QV ELF202, Kanagawa, Japan). Then, the images were analyzed with an image processing software (ImageJ, U.S. National Institutes of Health, Bethesda, Maryland, USA) to characterize relative density (ρ), used as a quantitative indicator of porosity distribution, as typically performed in the

Table 1. Fixed and varied parameters used in the investigation of LPBF processability of Fe2.9wt.%Si.

Fixed parameters	
Hatch distance, h_d, (μm)	70
Layer thickness, z, (μm)	30
Hatching rotation, (°)	67
Hatching strategy	Bidirectional
Inert gas type	Ar
Varied parameters	
Laser power, P, (W)	150, 200
Scan speed, v, (mm s^{-1})	700, 800, 900, 1000, 1100, 1200

literature [49]. Each ρ estimation is based on a filtering procedure which allows to binarize the cross section thus converting solid regions and pores with binary colors. The calculation of ρ then comes as follow:

$$\rho\,(\%) = \left(1 - \frac{A_{\text{pore,tot}}}{A_{\text{tot}}}\right) \cdot 100\% \tag{2}$$

where $A_{\text{pore,tot}}$ is the total area of the pores and A_{tot}, which is the total area of the section (bulk and pores). To compare different theoretical energy inputs depending on the choice of process parameters, the volumetric energy density, E (J mm^{-3}) was calculated with the following formula:

$$E(J) = \frac{P}{vzh_d} \tag{3}$$

where P, v, z and h_d are laser power, scan speed, layer thickness and hatch distance, respectively.

The condition producing adequate density was further analyzed in terms of microstructure and electromagnetic properties in as-built and heat treated conditions. Heat treatment consisted of annealing at 1200 °C for 1 h and under vacuum to improve the magnetic properties [38, 40, 50]. Microstructure was analyzed with optical microscopy after a chemical etching with Nital 2%. From the microstructures, grain size measurements in terms minor axis, d_{min} (μm) and major axis, d_{max} (μm) were acquired to calculate the grain aspect ratio (AR) (-) with the following formula:

$$AR = d_{\text{max}}/d_{\text{min}}\,. \tag{4}$$

Grain size defined with AR index is used in the literature to get insights about the morphology of the microstructure. According to the previous definition, when AR is less than 2, grain appear following an equiaxed fashion within the microstructure [51].

X-rays diffraction (XRD) patterns were recorded using a system (PW1830 from Philips, Almelo, The Netherlands) with Cu Kα ($\lambda = 1.5418$ Å) radiation. Diffraction peaks in the range $2\theta = [20°, 90°]$ were considered to determine the solid phase distribution. For each acquisition a step size and time of $\Delta 2\theta = 0.026°$ and $\Delta t = 82.62$ s were used. The analysis was conducted on the three representative specimens, namely on Fe2.9wt.%Si before and after heat treatment and the Zn-coated mild steel condition.

3.5. Specimen manufacturing and characterization of the magnetic properties

The toroidal samples and magnetic shields were produced via LPBF process using the most suitable process parameters that guaranteed adequate densification (>99.9%) as investigated from the preliminary experimental campaign.

Toroid samples were produced to test the electromagnetic properties in as-built and heat treated conditions. The so called 'O-ring test' in which the B–H curve for the material before and after the heat-treatment was evaluated at 10, 20, 30, 40, 50, 60, 100, 500, 1000 Hz [28].

Ferromagnetic shield consisted of a prismatic sample with main dimensions of 41.5 (l) × 17.5 (w) × 26.8 (h) mm^3, hollow with wall thickness (t) of 1 mm, as depicted in figure 3. The nominal dimensions of the shield are based on an actual conductive shield of a relé application. The conventional device made of Zn-coated mild steel was produced by bending 1 mm thick sheet. Two shields were produced by LPBF to test the electromagnetic shielding performances in the as-built and heat treated conditions.

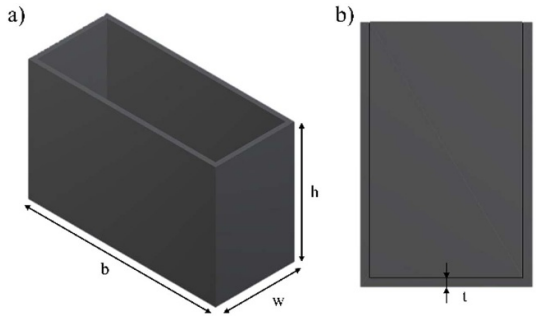

Figure 3. (a) Isometric view and (b) top view of the shield.

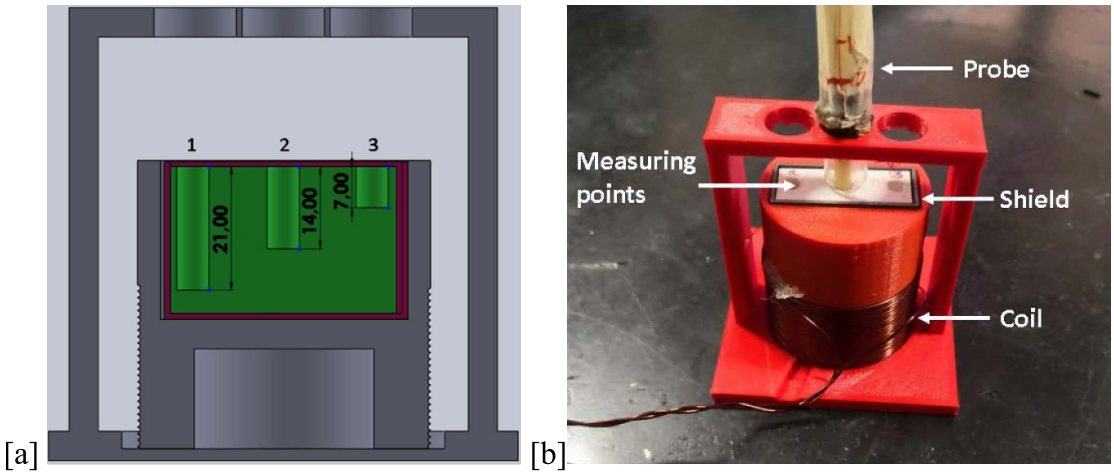

Figure 4. Overview of (a) the magnetic shielding characterization setup and (b) the measuring points within the shield.

3.6. Characterization of the shielding factor

Each shield was characterized using two different sources of magnetic field excitation DC and AC/DC considering two different orientations Z and Y as described in figure 4. The structure used for the measurements is shown in figure 4(a). An ad hoc PLA structure was produced using fused filament fabrication technique [52] to host the shields. This structure can be divided in three sections described as follows:

- The base part, which is the area where the generation of the field takes place. Figure 4 shows the coil for the AC/DC power supply. Instead, for the DC characterization, a permanent magnet was conveniently inserted in the center of the structure.
- The central part left hollow for the positioning of the shield.
- The upper part, which is characterized by holes aligned with the chosen measurement points for the insertion of the magnetic field probe.

In the case of an alternating magnetic field, the SF index was evaluated for different values of frequencies, namely 10, 20, 30, 40, 50, 60, 100, 500, 1000 Hz with a current equal to 2 A.

The reported results are calculated for each of the three configurations: traditionally manufactured ferritic steel shield (Zn-coated mild steel), additively manufactured ferromagnetic shield (Fe2.9wt.%Si As-built), and additively manufactured ferromagnetic shield after heat treatment (Fe2.9wt.%Si HT). A special prismatic sample was created and inserted inside the shield with three different measurement points characterized by different heights and positions to evaluate the shielding factor of this material, as shown in the figure 7.

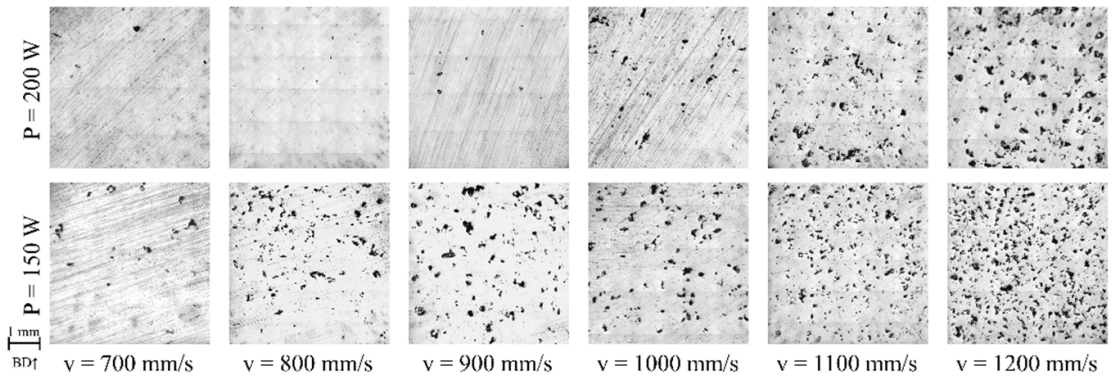

Figure 5. Metallographic cross sections comparison of the tested conditions. 'BD' stands for build direction.

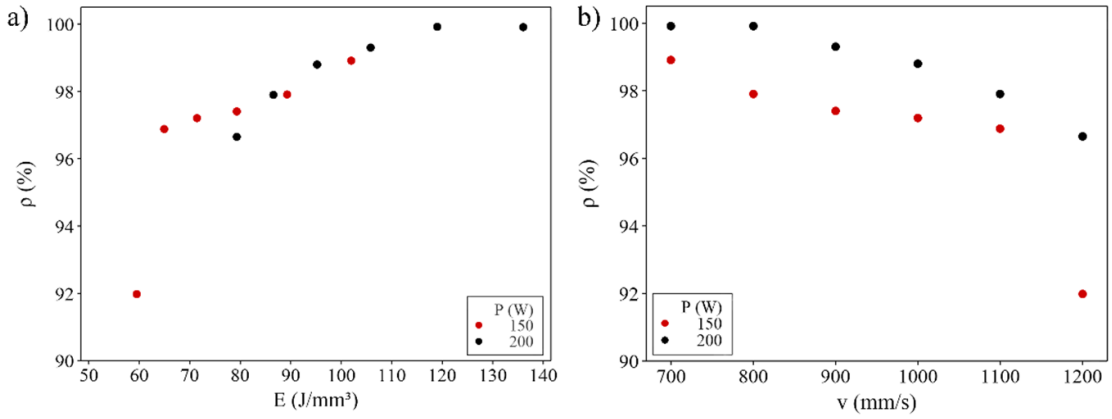

Figure 6. Relative density measurements (ρ) as a function of (a) energy density (E) and (b) process parameters (P, v).

4. Results

4.1. LPBF processability of Fe2.9 wt.%Si alloy

Figure 5 shows the metallographic cross section comparison of the tested conditions as a function of laser power and scan speed, as described in table 1. At $P = 150$ W, lack of fusion pores were observed irrespective of the scan speed level whereas at $P = 200$ W, highly dense cross sections were observed for the lower scan speed levels tested (700–900 mm s^{-1}). Figure 6 shows the relative density (ρ) of the experimented conditions as a function of the volumetric energy density (E) and scan speed (v), respectively. As appears from figure 6(a), the typical rising trends of ρ can be observed as a function of E. At $P = 200$ W, the trend stabilizes for $E > 110$ J mm^{-3} where adequate dense samples were manufactured ($\rho > 99.5\%$). Below this threshold ρ does not overcome 99% as an effect of insufficient energy input to fully melt the material. Similar trend can be observed from figure 6(b) in terms of scan speed. Indeed, high productive conditions featured by higher scan speeds ($v > 900$ mm s^{-1}) do not match adequate part quality in terms of relative density when working with $P = 200$ W. Instead, at $P = 150$ W, it is likely that even slower experimental conditions ($v < 700$ mm s^{-1}) would lead to adequate densification, even though not tested throughout this work.

For $P = 200$ W and $v = 800$ mm s^{-1}, the densest condition was measured with $\rho > 99.9\%$. Hence, this condition was selected for the manufacturing of shields along with the fixed hatch distance and layer thickness, of 70 and 30 μm, respectively, and the scanning strategy, namely bidirectional with a hatch rotation of 67° layer by layer. Figure 7 shows the test samples used for this work.

4.2. Microstructure

Figures 8(a) and (b) shows the microstructures of Fe2.9wt.%Si for the as-built condition and after heat treatment, respectively, along the build direction. As appears, the microstructure of the as-built sample was made of highly columnar and elongated grains along the build direction, which coincided with the direction of the heat flow during LPBF process. Heat treatment led to a significant grain morphology change. Indeed, grain structure appeared dominated by coarser and larger grains stretched along the build direction, mixed

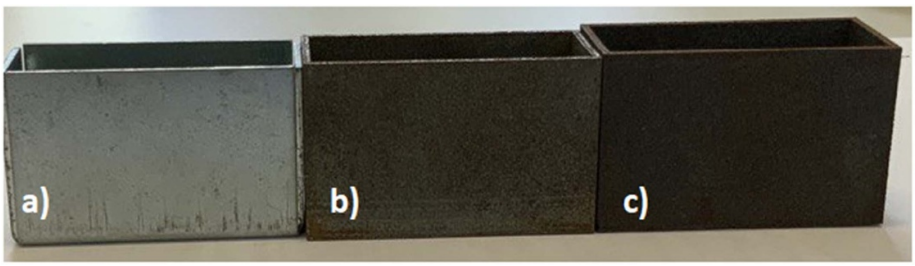

Figure 7. Electromagnetic shield samples: (a) Zn-coated mild steel, (b) Fe2.9wt.%Si As-built, (c) Fe2.9wt.%Si HT.

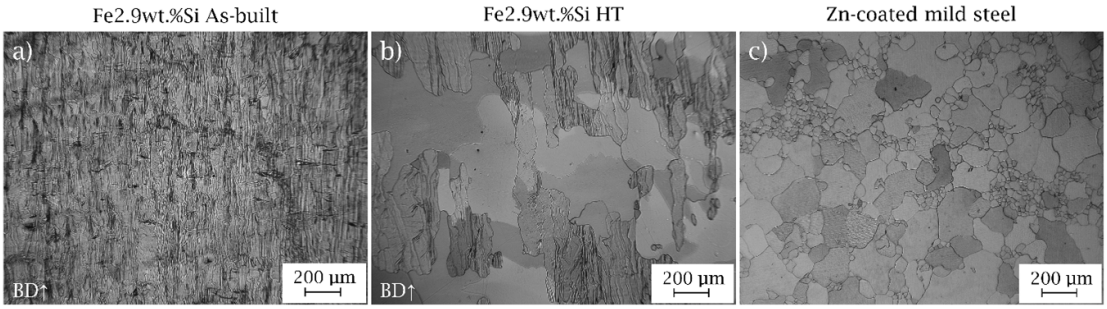

Figure 8. Optical microscopy of (a) Fe2.9 wt.%Si As-built, (b) Fe2.9 wt.%Si HT and (c) Zn-coated mild steel microstructures. BD stands for build direction.

Table 2. Measured grain major axis, d_{max} (μm), minor axis, d_{min}(μm), and aspect ratio, AR (-) in terms of mean and standard deviation for the FeSi2.9wt.%Si conditions (before and after heat treatment) and the reference Zn-coated mild steel condition.

Condition	d_{max} (μm)	d_{min} (μm)	AR (-)
Fe2.9wt.%Si As-built	317 ± 91	46 ± 17	7.2 ± 2
Fe2.9wt.%Si HT	210 ± 131	95 ± 69	2.4 ± 1
Zn-coated mild steel	141 ± 115	116 ± 93	1.2 ± 0.2

with smaller columnar grains. Overall, heat treatment led to a significant grain growth and a reduction of grain boundaries within the volume. This may be beneficial in terms of magnetic properties since grain boundaries may act as pin walls for magnetic domains thus limiting the magnetic properties. Quantitative measurements of grain minor axis (d_{min}), major axis (d_{max}), and AR are provided in table 2 in terms of mean and standard deviation for both the two tested conditions. As appears, grain size data in terms of d_{min} and d_{max} suffer from high variability because of the various grain morphologies encountered. Nonetheless, the AR index showed a significant reduction after heat treatment, from an average of 7.2–2.4. This implicitly demonstrates that grains reached a better equiaxed shape since the accepted technological threshold to pass from columnar to equiaxed grain morphology is an AR of 2 [51].

In contrast, the reference condition of Zn-coated mild steel appeared to be dominated by an equiaxed microstructure, as shown in figure 8(c). The microstructure is organized in clusters of smaller grains mixed with coarser and larger grains. Despite the high variability in the major and minor axes of the grains, the morphology generally resembles an equiaxed structure. This equiaxed morphology is confirmed by grain size measurements, with an average AR of approximately 1.2, as illustrated in table 2. The microstructure depicted in figure 8(c) shows the typical form of the ferritic mild steel [53–55].

The XRD results for Fe2.9wt.%Si As-built, Fe2.9wt.%Si HT and Zn-coated mild steel are presented in figure 9. Overall, the diffraction peaks of the bcc structure associated to the α phase can be observed for each of the tested condition, confirming the results from the literature [31, 37, 38]. Samples made of Fe2.9wt.%Si feature a single α phase that did not change after annealing. An increase of relative intensity of the diffraction peaks associated to Fe(200) and Fe(211) family planes suggested that annealing induced a moderate increase of <200> and <211> texture. This effect is related to the change of microstructure morphology occurring during the heat treatment as an effect of recrystallization. A similar effect on texture was observed also by Stornelli *et al* [31] working with a similar alloy grade (Fe3wt.%Si). As illustrated in figure 9, the reference condition made of Zn-coated mild steel also shows the presence of other diffraction peaks of the hcp

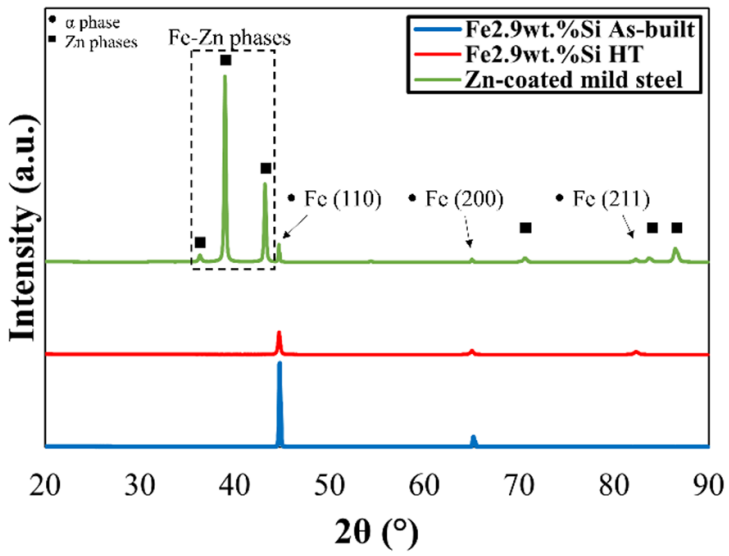

Figure 9. XRD spectra for Fe2.9wt.%Si As-built, Fe2.9wt.%Si HT samples and Zn-coated mild steel.

structure associated to the Zn-coating film shielding the mild steel core or other intermetallic phases containing Zn [56].

4.3. Permeability and B–H characterization

Figures 10 and 11 depict the electromagnetic characterization results of LPBF produced as-built and heat treated samples respectively. As can be seen from the graphs, the heat treatment at 1200 °C brought benefits to the magnetic properties. For all the frequencies studied there is an increase in the permeability values as reported in figure 10(a). The data of these characterizations were inserted in the simulation to evaluate the performance of the electromagnetic shield.

4.4. DC magnetic field excitation

The anisotropic characteristic of the materials was noticed in both the excitation directions, as appears from figure 12. Each value indicated for the different survey points represents the average of three measurements carried out for each condition. This behavior can be explained by the coincidence between the sample growth direction and the direction of easy magnetization of the material, as demonstrated in [39], as well as the anisotropy observed in the microstructure morphology. So, the SF values of the axial direction were much higher than in the transverse direction. Along both directions, there is a slight difference between the as-built and the reference shields made by Fe2.9wt.%Si and Zn-coated mild steel, respectively. Although, along the axial direction (Z) the Zn-coated mild steel shield performed better than the Fe2.9wt.%Si one, the opposite trend holds along the transverse direction (Y), for each of the measurement point. Instead, the heat treated condition outperformed the other two in each of the measurement point considered, especially in point 1, which is the deepest and therefore the closest to the shield. This type of heat treatment can increase the electrical and magnetic properties, particularly the permeability of the piece due to the microstructural change, as reported in [28], thus favoring an increase in the shielding properties.

4.5. AC/DC magnetic field excitation

Figures 13 and 14 show the SF measurements under AC/DC magnetic field excitation, for the axial (Z) and transverse (Y) directions respectively, for each measurement point and for various operating frequencies. Each value indicated for the different survey points represents the average of three measurements carried out for each condition. As appears from the acquisitions along the axial direction, the Zn-coated mild steel sample showed slightly higher SF values than the Fe2.9wt.%Si HT shield for point 1 and 2, whereas the opposite trend holds for point 3. In any measurement point, the as-built sample showed the lowest performances among the others. If selecting only the low-frequency spectrum ($>$200 Hz), the annealing treatment allowed to attain comparable results with the standard reference of Zn-coated mild steel. Instead, along the transverse direction, Zn-coated mild steel shield was always outperformed by the Fe2.9wt.%Si HT condition. Indeed, the SF values were always below those of the heat treated condition for any measurement point and for any tested frequency.

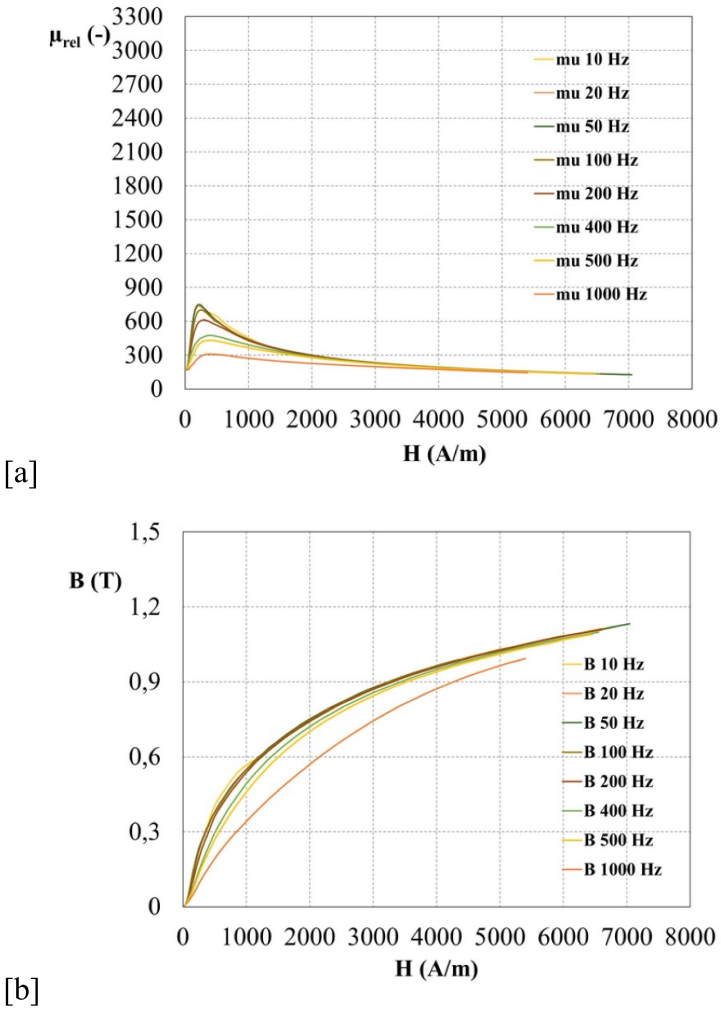

Figure 10. Electromagnetic properties of the Fe2.9wt.%Si As-built condition. (a) Relative permeability of the sample and (b) *B–H* characteristic of the sample for different frequencies.

Additional considerations can be made regarding the effect of eddy currents. Indeed, their presence, which is usually considered as losses, helped to increase the shielding factor. Moreover, for the case of axial measurement in AC/DC, referred to as measurement point 3 it is possible to notice a different trend compared to the previous points. This inversion can be explained because point 3 is located near the edge of the shield. Therefore, in addition to the dissipative effect of eddy currents, the effects at the edges increase the shielding factor at that point. Finally, considering the transversal cases carried out in AC/DC, it is possible to conclude that in this direction the eddy current losses are higher than the axial cases. Therefore, both in the as-built and heat treated conditions there is a more significant shielding factor. This behavior might be related to a different microstructure morphology between the walls and the base of the shield. In addition, the form factor must be considered which affects these types of measurements.

5. Discussion

The magnetic characterization based on the SF index allowed to demonstrate that even starting from an elementary shield geometry inspired by a relé application, the LPBF process allowed to build ferromagnetic shields with similar performances of those fabricated with a standard approach that consists in folding a 1 mm sheet Zn-coated mild steel. The present work demonstrated that as-built shields should undergo a further annealing heat treatment to match the adequate shielding performances, as also demonstrated in a previous work [28] for other magnetic properties, like permeability or specific iron losses. This is because, as demonstrated in reference [28], after the heat treatment there is an increase in the permeability of the material so that the magnetic field lines tend to be bounded easily in the piece. Once heat treatment is performed, the microstructure changes from a columnar-dominated grain fashion to a mixture of large and coarse grains still stretched along the build direction and residues of columnar grains from the as-built

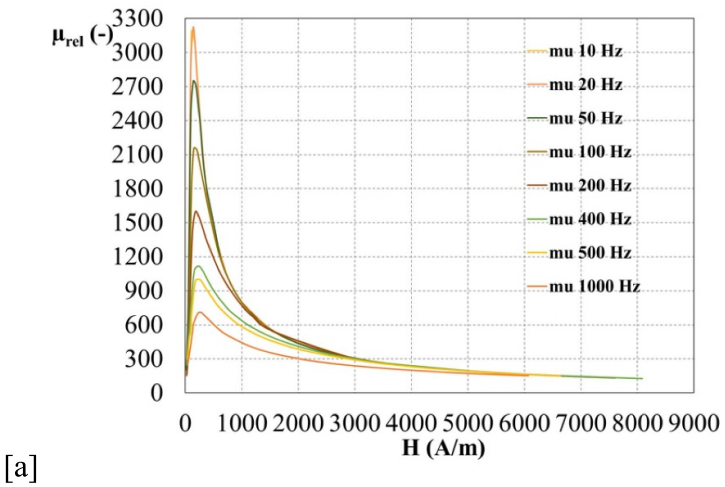

[a]

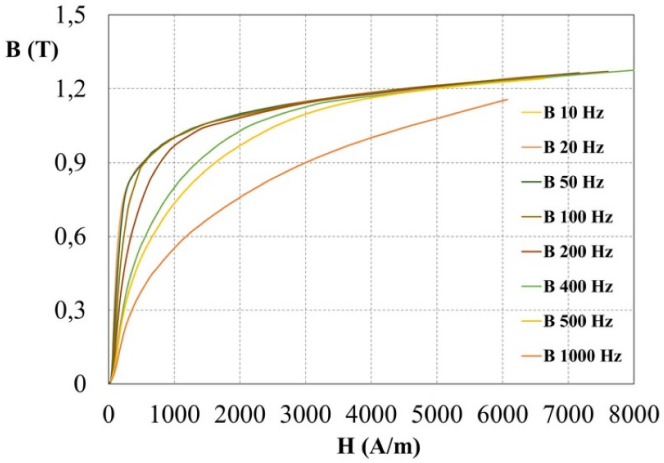

[b]

Figure 11. Electromagnetic properties of the Fe2.9wt.%Si HT condition. (a) Relative permeability of the sample and (b) *B–H* characteristic of the sample for different frequencies.

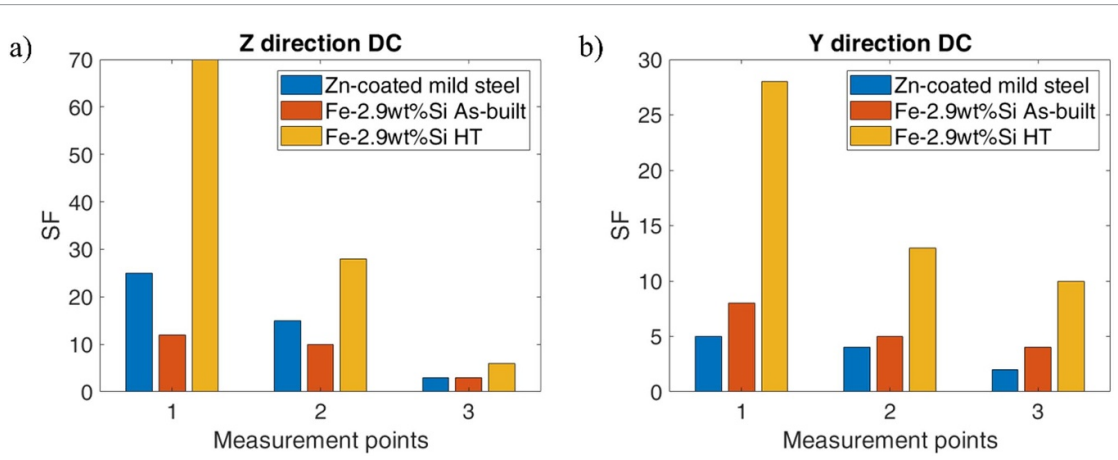

Figure 12. SF values along the axial (a) and transversal (b) direction for the three different measurement points, DC excitation.

condition. However, the key-role of the heat treatment seems to be the change of grain size and morphology rather than the directionality, since the SF results revealed the anisotropic magnetic behavior of the alloy both before and after the thermal treatment. Nonetheless, the macro views of the microstructure revealed that the heat treatment might need further improvements since islands of columnar grains residues, that did not undergo recrystallization during annealing, are still present after heat treatment. With the proper tuning

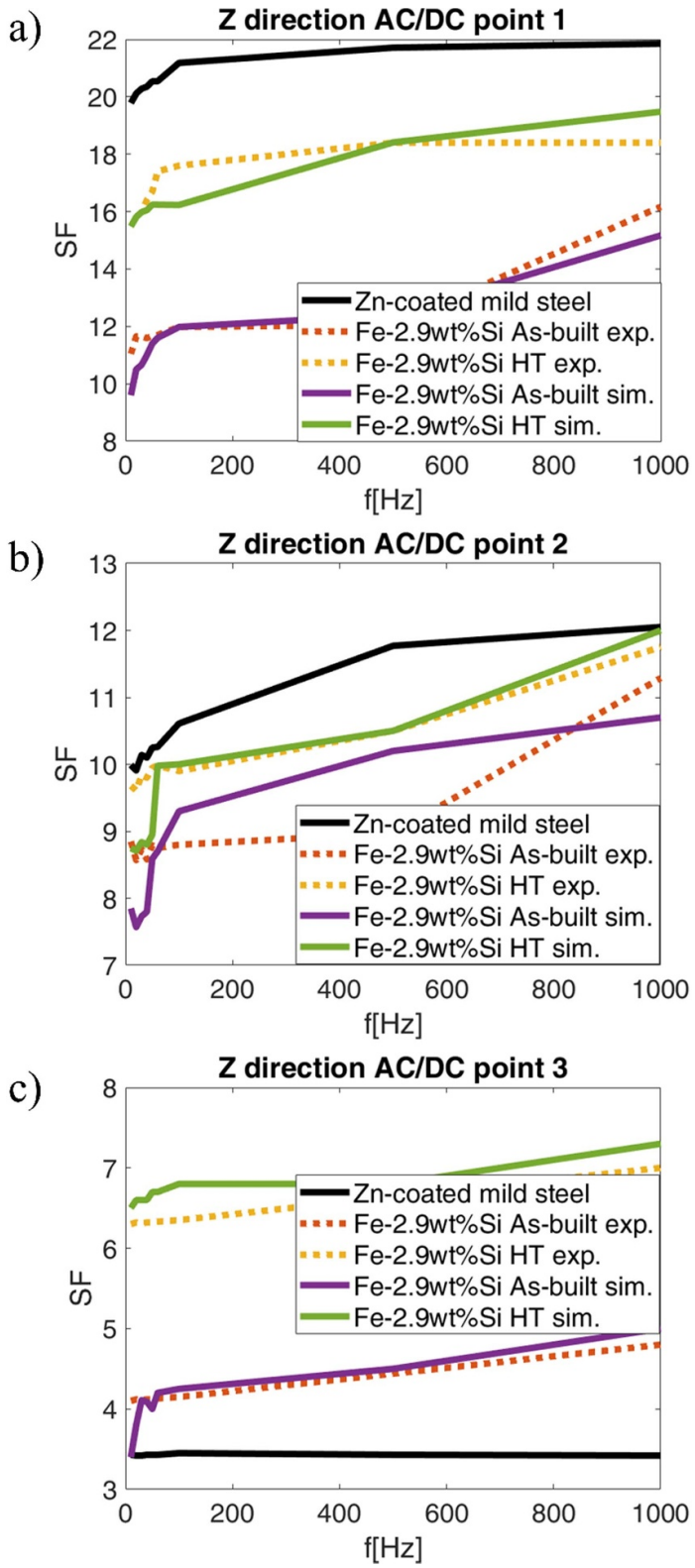

Figure 13. Comparison between SF values simulated and experimental evaluated along the axial direction for the three different measurement points, AC/DC excitation.

of laser power and scan speed, highly dense shields (>99.9%) were built, and under DC magnetic field excitation the SF factor of the heat treated condition outclasses the other tested conditions in any measurement point and along any of the two tested directions (axial and transverse). Instead, under AC/DC excitation field, the magnetic shielding performances of the heat treated condition are better than the Zn-coated mild steel only on the transverse direction, for any of the tested frequency and measurement point. On the contrary, along the axial direction, the standard Zn-coated mild steel shield shows comparable

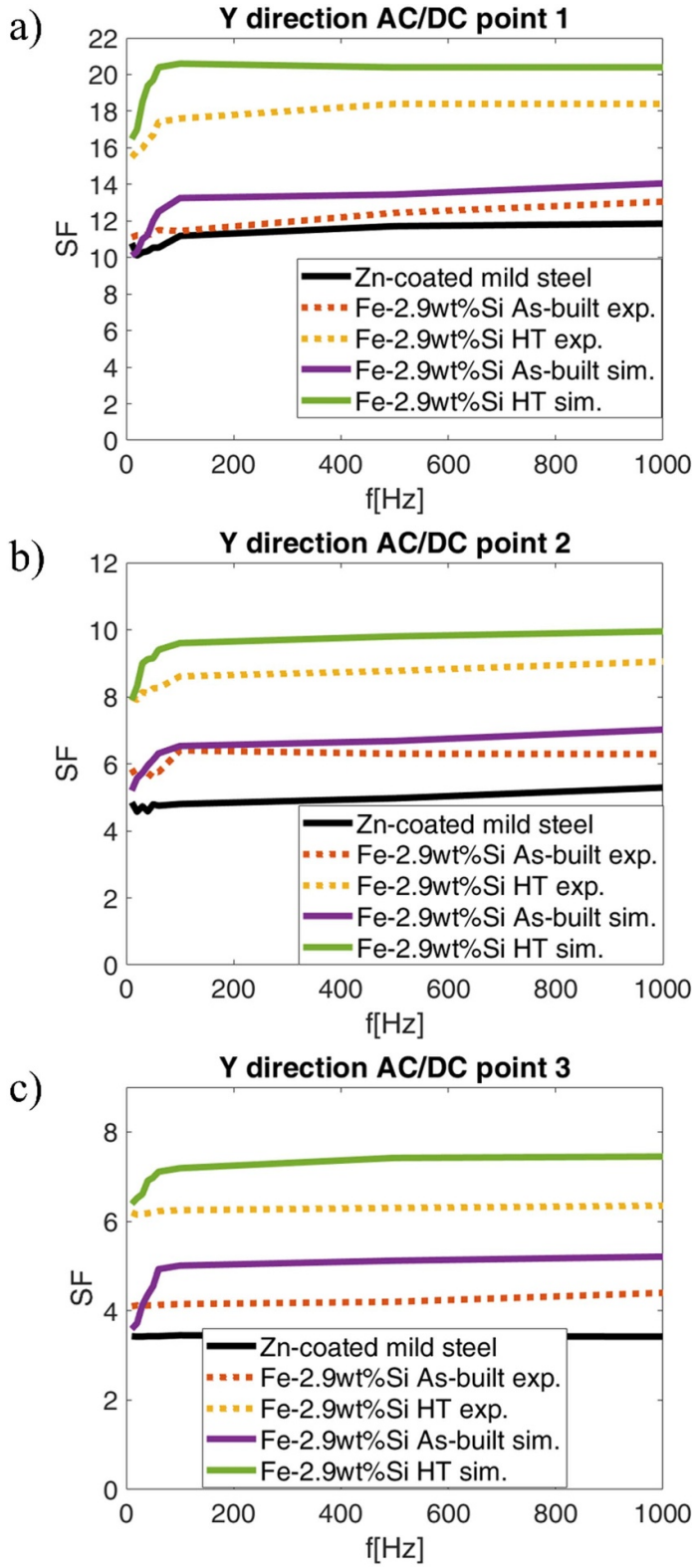

Figure 14. Comparison between SF values simulated and experimental evaluated along the transverse direction for the three different measurement points, AC/DC excitation.

but slightly better shielding performances than the heat treated condition only at the bottom and at the half of the shield (first two measurement points). Testing of magnetic shielding performances of functional and practical samples made via LPBF is not very common [43–45]. This work demonstrated that LPBF is suitable for the manufacturing of iron silicon steel shields even with elementary geometries, while TLPBF offers a great freedom in the design of functional components. Complex 3D structures, such as lattice structures, can

be addressed to tailor the magnetic flux according to the applications, i.e. foster the trapping of magnetic field lines within the conductor for shielding applications.

6. Conclusions

In this work, the magnetic shielding performances of two Fe2.9wt.%Si based shields produced with LPBF were compared with a Zn-coated mild steel shield reference. Optimized process parameters were chosen to guarantee adequate densification (>99.9%) to the as-built samples, as demonstrated from an explorative experimental campaign focused on the understanding of the feasibility window of the processed alloy. The LPBF produced shield was further subjected to heat treatment to match the correct magnetic performances for the tested iron silicon grade. Shielding Factor was evaluated under different magnetic field excitation modes, DC vs AC/DC, directions, axial and transverse, in different points and under different operating frequencies. Additional microstructure and grain size characterization were performed to better comprehend the effect of heat treatment on magnetic shielding performance. The results demonstrated that the heat treated Fe2.9wt.%Si sample produced with LPBF can outperform the Zn-coated mild steel standard in terms of shielding performances under stationary conditions (DC). Under alternating current (AC/DC), the shielding performances of the heat treated sample are slightly lower but comparable with the standard Fe-based shield. Different shielding performances were noticed in the two magnetic field directions because of the anisotropic behaviour of the material as observed from the microstructure characterization. Overall, the work demonstrates that shields made of simple geometries via LPBF with Fe2.9 wt.%Si alloy can substitute the reference made by Zn-coated mild steel in terms of magnetic shielding performances. However, to meet adequate magnetic performances, the as-built samples still require an annealing heat treatment. The results highlight the potential of using AM for the production of electromagnetic shields customized to the specific application. Future works will focus on the realization of more complex geometries enabled by the LPBF process, for instance acting on topological optimized or lattice structures to enhance the magnetic field shielding of as-built samples.

Data availability statement

All data that support the findings of this study are included within the article (and any supplementary files).

ORCID iDs

Michele Quercio https://orcid.org/0000-0001-8086-6979
Francesco Galbusera https://orcid.org/0000-0003-0293-8636
Aldo Canova https://orcid.org/0000-0002-0014-5918
Ali Gökhan Demir https://orcid.org/0000-0002-8000-468X
Giambattista Gruosso https://orcid.org/0000-0001-6417-3750
Barbara Previtali https://orcid.org/0000-0002-6074-8753

References

[1] Tofail S A M, Koumoulos E P, Bandyopadhyay A, Bose S, O'Donoghue L and Charitidis C 2018 Additive manufacturing: scientific and technological challenges, market uptake and opportunities *Mater. Today* **21** 22–37
[2] Altıparmak S C and Xiao B 2021 A market assessment of additive manufacturing potential for the aerospace industry *J. Manuf. Process.* **68** 728–38
[3] Lamichhane T N, Sethuraman L, Dalagan A, Wang H, Keller J and Paranthaman M P 2020 Additive manufacturing of soft magnets for electrical machines—a review *Mater. Today Phys.* **15** 100255
[4] Selema A, Ibrahim M N and Sergeant P 2022 Metal additive manufacturing for electrical machines: technology review and latest advancements *Energies* **15** 1076
[5] Naseer M U, Kallaste A, Asad B, Vaimann T and Rassõlkin A 2021 A review on additive manufacturing possibilities for electrical machines *Energies* **14** 1940
[6] Szabó L and Fodor D 2022 The key role of 3D printing technologies in the further development of electrical machines *Machines* **10** 0–29
[7] Wrobel R and Mecrow B 2020 A comprehensive review of additive manufacturing in construction of electrical machines *IEEE Trans. Energy Convers.* **35** 1054–64
[8] Tiismus H, Kallaste A, Vaimann T and Rassõlkin A 2022 State of the art of additively manufactured electromagnetic materials for topology optimized electrical machines *Addit. Manuf.* **55** 102778
[9] Bräuer P *et al* 2012 3D screen printing technology-opportunities to use revolutionary materials and machine designs *2012 2nd Int. Electric Drives Production Conf., EDPC 2012—Proc.* (https://doi.org/10.1109/EDPC.2012.6425124)
[10] Li Y *et al* 2023 3D-printed magnetic porous structures with different Poisson's ratios and their mechanoelectrical conversion capabilities *Addit. Manuf.* **69** 103542
[11] Magisetty R P and Cheekuramelli N S 2019 Additive manufacturing technology empowered complex electromechanical energy conversion devices and transformers *Appl. Mater. Today* **14** 35–50

[12] O'Donnell J, Kim M and Yoon H S 2017 A review on electromechanical devices fabricated by additive manufacturing *Trans. ASME, J. Manuf. Sci. Eng.* **139** 010801
[13] Ramos J *et al* 3D printing of electro mechanical systems (available at: www.researchgate.net/publication/289151566)
[14] Pham T Q, Do T T, Kwon P and Foster S N 2018 Additive manufacturing of high performance ferromagnetic materials *2018 IEEE Energy Conversion Congress and Exposition, ECCE* (*December 2018*) (Institute of Electrical and Electronics Engineers Inc) pp 4303–8
[15] Liu C 2018 Emerging electric machines and drives—an overview *IEEE Trans. Energy Convers.* **33** 2270–80
[16] Lammers S *et al* 2016 Additive manufacturing of a lightweight rotor for a permanent magnet synchronous machine *2016 6th Int. Electric Drives Production Conf., EDPC 2016—Proc.* (Institute of Electrical and Electronics Engineers Inc) pp 41–45
[17] Zhang Z Y, Jhong K J, Cheng C W, Huang P W, Tsai M C and Lee W H 2016 Metal 3D printing of synchronous reluctance motor *Proc. IEEE Int. Conf. on Industrial Technology* (*May*) (Institute of Electrical and Electronics Engineers Inc) pp 1125–8
[18] Huang P W, Jiang I H, Tsai M C and Chen G M 2019 New hybrid stator design for high-speed PMSMS based on selective laser melting of 3D printing *IEEE Trans. Magn.* **55** 1–4
[19] Lamichhane T N *et al* 2022 Additively manufactured Fe-3Si stator for high-performance electrical motor (available at: https://ssrn.com/abstract=4086824)
[20] Plotkowski A, Carver K, List F, Pries J, Li Z, Rossy A M and Leonard D 2020 Design and performance of an additively manufactured high-Si transformer core *Mater. Des.* **194** 108894
[21] Tiismus H, Kallaste A, Belahcen A, Rassõlkin A, Vaimann T and Ghahfarokhi P S 2021 Additive manufacturing and performance of E-type transformer core *Energies* **14** 3278
[22] Plotkowski A *et al* 2019 Influence of scan pattern and geometry on the microstructure and soft-magnetic performance of additively manufactured Fe-Si *Addit. Manuf.* **29** 100781
[23] Koo B, Jang M-S, Nam Y G, Yang S, Yu J, Park Y H and Jeong J W 2021 Structurally-layered soft magnetic Fe-Si components with surface insulation prepared by shell-shaping selective laser melting *Appl. Surf. Sci.* **553** 149510
[24] Gao S, Yan X, Chang C, Aubry E, Liu M, Liao H and Fenineche N 2021 Effect of laser energy density on surface morphology, microstructure, and magnetic properties of selective laser melted Fe-3wt.% Si alloys *J. Mater. Eng. Perform.* **30** 5020–30
[25] Nakajima K, Leparoux M, Kurita H, Lanfant B, Cui D, Watanabe M, Sato T and Narita F 2022 Additive manufacturing of magnetostrictive Fe–Co alloys *Materials* **15** 709
[26] Chaudhary V, Sai Kiran Kumar Yadav N M, Mantri S A, Dasari S, Jagetia A, Ramanujan R V and Banerjee R 2020 Additive manufacturing of functionally graded Co–Fe and Ni–Fe magnetic materials *J. Alloys Compd.* **823** 153817
[27] Chaudhary V, Mantri S A, Ramanujan R V and Banerjee R 2020 Additive manufacturing of magnetic materials *Prog. Mater. Sci.* **114** 100688
[28] Quercio M *et al* 2022 Functional characterization of L-PBF produced FeSi2.9 soft magnetic material *2022 Int. Conf. on Electrical Machines, ICEM* (https://doi.org/10.1109/ICEM51905.2022.9910684)
[29] Urbanek S *et al* 2021 Design and experimental investigation of an additively manufactured PMSM rotor *2021 IEEE Int. Electric Machines and Drives Conf., IEMDC 2021* (Institute of Electrical and Electronics Engineers Inc) (https://doi.org/10.1109/IEMDC47953.2021.9449566)
[30] Urbanek S *et al* 2018 Additive manufacturing of a soft magnetic rotor active part and shaft for a permanent magnet synchronous machine *2018 IEEE Transportation and Electrification Conf. and Expo, ITEC 2018* (Institute of Electrical and Electronics Engineers Inc) pp 217–9
[31] Stornelli G, Faba A, Di Schino A, Folgarait P, Ridolfi M R, Cardelli E and Montanari R 2021 Properties of additively manufactured electric steel powder cores with increased Si content *Materials* **14** 1489
[32] Tiismus H, Kallaste A, Naseer M U, Vaimann T and Rassolkin A 2022 Design and performance of laser additively manufactured core induction motor *IEEE Access* **10** 50137–52
[33] Tiismus H *et al* 2022 Laser additively manufactured magnetic core design and process for electrical machine applications *Energies* **15** 3665
[34] Goodall A D, Chechik L, Mitchell R L, Jewell G W and Todd I 2023 Cracking of soft magnetic FeSi to reduce eddy current losses in stator cores *Addit. Manuf.* **70** 103555
[35] Urban N, Bauch L, Armbruster R and Franke J 2019 Evaluation of soft magnetic ferrosilicon FeSi 6.5 for laser beam melting *2019 9th Int. Electric Drives Production Conf., EDPC 2019—Proc.* pp 2019–22
[36] Goll D *et al* 2019 Additive manufacturing of soft magnetic materials and components *Addit. Manuf.* **27** 428–39
[37] Garibaldi M, Ashcroft I, Simonelli M and Hague R 2016 Metallurgy of high-silicon steel parts produced using selective laser melting *Acta Mater.* **110** 207–16
[38] Garibaldi M, Ashcroft I, Lemke J N, Simonelli M and Hague R 2018 Effect of annealing on the microstructure and magnetic properties of soft magnetic Fe-Si produced via laser additive manufacturing *Scr. Mater.* **142** 121–5
[39] Garibaldi M, Ashcroft I, Hillier N, Harmon S A C and Hague R 2018 Relationship between laser energy input, microstructures and magnetic properties of selective laser melted Fe-6.9%wt Si soft magnets *Mater. Charact.* **143** 144–51
[40] Lemke J N, Simonelli M, Garibaldi M, Ashcroft I, Hague R and Vedani M 2017 Calorimetric study and microstructure analysis of the order-disorder phase transformation in silicon steel built by SLM *J. Alloys Compd.* **722** 293–301
[41] Gargalis L, Madonna V, Giangrande P, Rocca R, Hardy M, Ashcroft I, Galea M and Hague R 2020 Additive manufacturing and testing of a soft magnetic rotor for a switched reluctance motor *IEEE Access* **8** 206982–91
[42] Garibaldi M, Gerada C, Ashcroft I and Hague R 2019 Free-form design of electrical machine rotor cores for production using additive manufacturing *Trans. ASME, J. Mech. Des.* **141** 071401
[43] Vovrosh J *et al* 2018 Additive manufacturing of magnetic shielding and ultra-high vacuum flange for cold atom sensors *Sci. Rep.* **8** 2023
[44] Mohamed A E M A, Sheridan R S, Bongs K and Attallah M M 2021 Microstructure-magnetic shielding development in additively manufactured Ni-Fe-Mo soft magnet alloy in the as fabricated and post-processed conditions *J. Alloys Compd.* **884** 161112
[45] Li B, Zhang W, Fu W and Xuan F 2023 Laser powder bed fusion (L-PBF) 3D printing thin overhang walls of permalloy for a modified honeycomb magnetic-shield structure *Thin-Walled Struct.* **182** 110185
[46] Li B, Zhang L, Fu W and Xu H 2020 General investigations on manufacturing quality of permalloy via selective laser melting for 3D printing of customized magnetic shields *JOM* **72** 2834–44
[47] Canova A and Quercio M 2023 A shielding system proposal for the cabling of electric glass melters *IEEE Open J. Ind. Appl.* **4** 1–10
[48] Canova A, Giaccone L and Quercio M 2021 A proposal for performance evaluation of low frequency shielding efficiency *CIRED 2021 - The 26th Int. Conf. and Exhibition on Electricity Distribution* pp 935–9

[49] Galbusera F, Demir A G, Platl J, Turk C, Schnitzer R and Previtali B 2022 Processability and cracking behaviour of novel high-alloyed tool steels processed by laser powder bed fusion *J. Mater. Process. Technol.* **302** 117435
[50] Shokrollahi H and Janghorban K 2007 Different annealing treatments for improvement of magnetic and electrical properties of soft magnetic composites *J. Magn. Magn. Mater.* **317** 61–67
[51] Biscuola V B and Martorano M A 2008 Mechanical blocking mechanism for the columnar to equiaxed transition *Metall. Mater. Trans. A* **39** 2885–95
[52] Vyavahare S, Teraiya S, Panghal D and Kumar S 2020 Fused deposition modelling: a review *Rapid Prototyp. J.* **26** 176–201
[53] Carluccio D, Bermingham M, Kent D, Demir A G, Previtali B and Dargusch M S 2019 Comparative study of pure iron manufactured by selective laser melting, laser metal deposition, and casting processes *Adv. Eng. Mater.* **21** 1900049
[54] Montani M, Demir A G, Mostaed E, Vedani M and Previtali B 2017 Processability of pure Zn and pure Fe by SLM for biodegradable metallic implant manufacturing *Rapid Prototyp. J.* **23** 514–23
[55] Krauss G 2018 Microstructures, processing, and properties of steels *Properties and Selection: Irons, Steels, and High-Performance Alloys* (ASM International) pp 126–39
[56] Vourlias G 2020 Application of x-rays diffraction for identifying thin oxide surface layers on zinc coatings *Coatings* **10** 1–14